

1
2
3
4
5
6
7
8
9
10
11
12
13
14
15
16
17
18
19
20
21
22
23
24
25
26
27
28
29
30
31
32
33
34
35
36
37
38
39
40
41
42
43
44
45
46
47
48
49
50
51
52
53
54
55
56
57
58
59
60

Nanoscale Colocalization of Fluorogenic Probes Reveals Role of Oxygen Vacancies in the Photocatalytic Activity of Tungsten Oxide Nanowires

Meikun Shen^{1†}, Tianben Ding^{2†}, Steven T. Hartman³, Fudong Wang¹, Christina Krucylak¹, Zheyu
Wang³, Che Tan⁴, Bo Yin³, Rohan Mishra^{3,5}, Matthew D. Lew^{2,3*}, Bryce Sadtler^{1,3*}

¹Department of Chemistry, Washington University, St. Louis, Missouri 63130

²Department of Electrical and Systems Engineering, Washington University, St. Louis, Missouri
63130

³Institute of Materials Science & Engineering, Washington University, St. Louis, Missouri 63130

⁴Department of Energy, Environmental & Chemical Engineering, Washington University, St.
Louis, Missouri 63130

⁵Department of Mechanical Engineering and Materials Science, Washington University, St.
Louis, Missouri 63130

[†]Denotes equal contribution

*To whom correspondence should be addressed. Email: mdlew@wustl.edu, sadtler@wustl.edu

Abstract

Defect engineering is a strategy that has been widely used to design active semiconductor photocatalysts. However, understanding the role of defects, such as oxygen vacancies, in controlling photocatalytic activity remains a challenge. Here we report the use of chemically-

1
2 triggered fluorogenic probes to study the spatial distribution of active regions in individual
3 tungsten oxide nanowires using super-resolution fluorescence microscopy. The nanowires show
4 significant heterogeneity along their lengths for the photocatalytic generation of hydroxyl radicals.
5
6 Through quantitative, coordinate-based colocalization of multiple probe molecules activated by
7 the same nanowires, we demonstrate that the nanoscale regions most active for the photocatalytic
8 generation of hydroxyl radicals also possess a greater concentration of oxygen vacancies.
9 Chemical modifications to remove or block access to surface oxygen vacancies, supported by
10 calculations of binding energies of adsorbates to different surface sites on tungsten oxide, show
11 how these defects control catalytic activity at both the ensemble and single-particle level. These
12 findings reveal that clusters of oxygen vacancies activate surface-adsorbed water molecules
13 towards photooxidation to produce hydroxyl radicals, a critical intermediate in several
14 photocatalytic reactions.
15
16

17 **Keywords:** tungsten oxide, oxygen vacancies, fluorescence, single-molecule localization
18 microscopy, colocalization
19
20

21 **Introduction**

22
23

24 Metal oxide semiconductors are promising photocatalysts for a number of important chemical
25 transformations including solar water splitting,¹⁻⁶ CO₂ reduction,⁶⁻⁹ coupling of amines,¹⁰⁻¹¹ and
26 the partial methane oxidation to produce methanol.¹²⁻¹³ They can be fabricated using inexpensive,
27 solution-phase synthesis, and they are more resistant to corrosion compared to elemental,
28 chalcogenide, and III-V semiconductors. However, as most metal oxides possess electronic
29 bandgap energies greater than 2.5 eV, their efficiency is limited by low absorption coefficients
30
31

1
2
3 where incoming solar radiation is most intense. Furthermore, due to low electron and hole
4 mobilities, photoexcited charge carriers have a high probability of recombining before they reach
5 the surface to oxidize or reduce adsorbed substrate molecules.^{6, 14-15} These limitations can be
6 mitigated if the surface of the photocatalyst possesses sites that are highly active for the chemical
7 transformation of interest.
8
9

10
11
12
13
14
15 The presence of structural defects, including vacancies, substitutional impurities, and
16 unpassivated atoms, at the surface of a semiconductor can introduce surface states within the band
17 gap that act as recombination centers and deactivate photoexcited charges. However, rather than
18 act as recombination centers, oxygen vacancies appear to enhance catalytic activity in many metal
19 oxide photocatalysts, including tungsten, indium, titanium, molybdenum, and zinc oxide.^{3-11, 16-20}
20
21 Several studies have reported higher catalytic activity in these materials as the oxygen vacancy
22 concentration is increased through thermal or chemical treatments, although various mechanisms
23 have been proposed to explain this observation.^{3-8, 10-11, 16} Density-functional-theory (DFT)
24 calculations suggest that oxygen vacancies act both as preferential adsorption sites for reactant
25 molecules and create new states within the electronic band gap of the semiconductor.^{4, 10} It is
26 currently debated whether or not charge carriers in these localized defect states can participate in
27 photochemical reactions.^{4-8, 10} Furthermore, the plasmon resonance induced by an increased free-
28 electron density increases absorption at longer wavelengths.^{5-6, 21} Currently, there is not a clear
29 consensus as to which of these mechanisms is dominant. A major obstacle in understanding the
30 role oxygen vacancies play in catalytic activity is that different metal oxide particles within a single
31 batch exhibit variations in the concentration and distribution of oxygen vacancies. This
32 heterogeneity makes it difficult to correlate specific morphological and structural features with
33 catalytic activity when measurements are made on large groups of particles. Thus, methods are
34
35
36
37
38
39
40
41
42
43
44
45
46
47
48
49
50
51
52
53
54
55
56
57
58
59
60

needed that can spatially map variations in activity for individual particles and correlate those variations with the specific structural features that lead to high or low activity.

Single-molecule imaging has been applied to study size and shape effects in chemical reactions catalyzed by inorganic nano- and microstructures, including metal nanoparticles,²²⁻³¹ layered and mesoporous materials,³¹⁻³⁴ metal oxides,^{31, 35-40} and metal–metal oxide heterostructures.^{31, 41-42} By localizing the positions of individual redox-active probe molecules that are chemically triggered by interfacial charge transfer, one can obtain a map of reaction events at the surface of these materials with nanoscale spatial resolution. Several studies have compared electron microscopy and single-molecule fluorescence images of the same catalyst particles to show that their activity can vary along a single crystal facet or in the regions between groups of closely-spaced particles. However, because the spatial resolution provided by this technique (typically 10 to 25 nm) still averages over many atoms on the surface of the catalyst, in most cases the chemical structure of the active regions could not be conclusively identified.^{23-28, 36-39}

In this report, we use single-molecule super-resolution imaging of chemically-activated molecular probes to map variations in the catalytic activity of tungsten oxide ($W_{18}O_{49}$) nanowires. Activation of the first probe molecule requires photoexcitation above the bandgap of the semiconductor to generate hydroxyl radicals. The second reaction does not require photoexcitation but instead relies on the presence of either oxygen vacancies or hydroxyl groups at the surface of the nanowires. Through quantitative colocalization of the spatial distribution of the two probes, we show that the nanowires contain inactive regions dispersed among segments that are catalytically active for both transformations. The high degree of spatial correlation between the two probe reactions enabled us to elucidate the structural nature of the active regions. Segments along each nanowire that contain clusters of oxygen vacancies activate surface-adsorbed water

1
2
3 molecules during the photocatalytic generation of hydroxyl radicals, an important intermediate in
4 the production of chemical fuels from sunlight.
5
6
7
8
9
10

11 Results and Discussion 12

13
14 **Oxygen vacancies in tungsten oxide nanowires.** $W_{18}O_{49}$ nanowires were synthesized using a
15 solvothermal method (see the **Supporting Information** for further details). An x-ray diffraction
16 pattern of the as-synthesized sample (**Figure S1**) matched the standard pattern for monoclinic
17 $W_{18}O_{49}$ (PDF card # 00-005-0392). Transmission electron microscopy (TEM) images show that
18 the nanowires possess an average diameter of 14 ± 8 nm (average $\pm 1^{\text{st}}$ standard deviation) and
19 lengths of several micrometers (**Figure 1a**). A high-resolution TEM (HRTEM) image (**Figure**
20
21 **1b**) of a section along a single nanowire shows lattice fringes with a spacing of 3.8 \AA aligned
22 perpendicular to the nanowire length. This lattice spacing matches the d-spacing for the (010)
23 plane of monoclinic $W_{18}O_{49}$, indicating the nanowire grew along the [010] direction (see **Figure**
24
25 **S2** for additional HRTEM images).^{19, 43}
26
27

28 The monoclinic phase of tungsten oxide corresponding to $W_{18}O_{49}$ can accommodate variations
29 in the W:O stoichiometry that arise due to oxygen vacancies.^{6, 21} Evidence of the presence of
30 oxygen vacancies in the as-synthesized $W_{18}O_{49}$ nanowires was provided by x-ray photoelectron
31 spectroscopy (XPS) (**Figure 1d**). The W 4f core level peaks obtained by XPS can be assigned to
32 a mixture of W^{6+} , W^{5+} , and W^{4+} .^{19, 44} Tungsten ions in the +5 and +4 oxidation states compensate
33 the positive charge left by the removal of O^{2-} . We also observe a shoulder peak in the region for
34 O 1s at a higher binding energy than the peak corresponding to lattice oxygen (**Figure S3**). This
35 peak has been previously attributed to surface-adsorbed oxygen species that bind to metal ions left
36
37

1
2
3 exposed by oxygen vacancies.^{9, 11, 19} Furthermore, the absorption spectrum of a film of W₁₈O₄₉
4 nanowires measured using an integrating sphere shows an absorption edge near 440 nm (**Figure**
5 **1e**), which corresponds to bandgap excitation of tungsten oxide (E_g = 2.8 eV). The broad
6 absorption at wavelengths beyond 500 nm has been previously attributed to free carrier absorption
7 induced by surface oxygen vacancies in W₁₈O₄₉.^{5-6, 21} Oxidation of the nanowires using either
8 hydrogen peroxide, H₂O₂, or thermal annealing in air led to the disappearance of free carrier
9 absorption (**Figure S4**). Oxidation using H₂O₂ preserved the monoclinic W₁₈O₄₉ phase of the
10 nanowires (**Figure S5**) enabling us to compare the catalytic activity of nanowires with and without
11 oxygen vacancies.
12
13
14
15
16
17
18
19
20
21
22
23
24
25
26
27
28
29
30
31
32
33
34
35
36
37
38
39
40
41
42
43
44
45
46
47
48
49
50
51
52
53
54
55
56
57
58
59
60

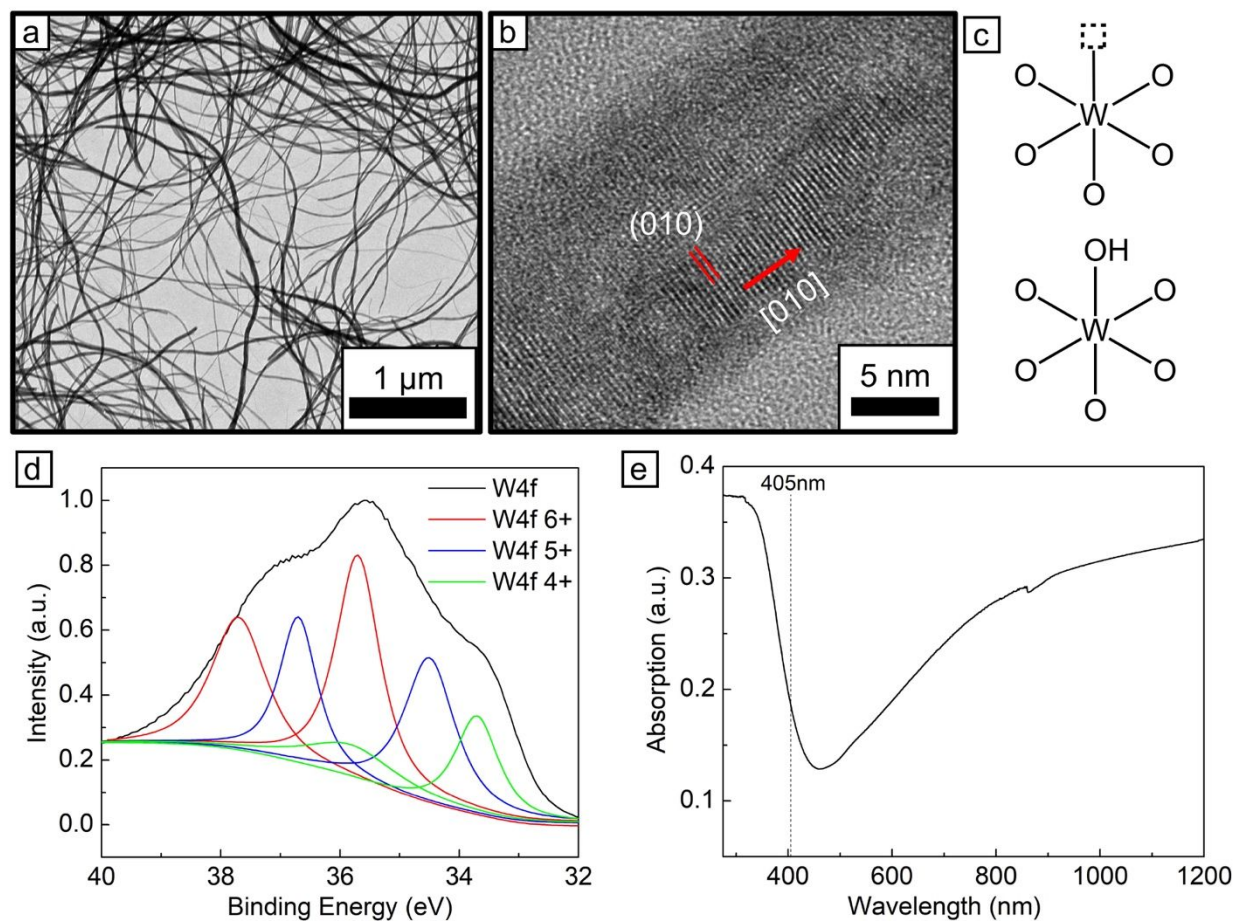


Figure 1. Structural characterization of $\text{W}_{18}\text{O}_{49}$ nanowires. (a) Low-magnification and (b) high-resolution TEM images of $\text{W}_{18}\text{O}_{49}$ nanowires. (c) Models for an oxygen vacancy (top) and a hydroxyl group (bottom) at the surface of $\text{W}_{18}\text{O}_{49}$. (d) X-ray photoelectron spectrum for $\text{W}_{18}\text{O}_{49}$ nanowires in the binding energy region for W 4f electrons. (e) Absorption spectrum of a dry film of $\text{W}_{18}\text{O}_{49}$ nanowires.

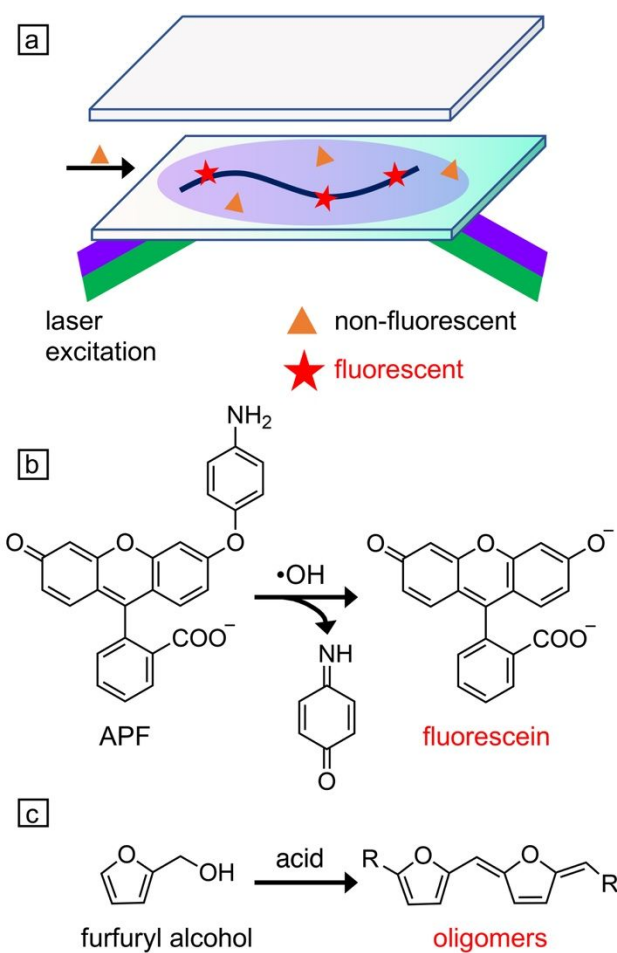


Figure 2. Single-molecule imaging of catalytic reactions using fluorogenic probes. (a) Experimental set-up for total internal reflection fluorescence (TIRF) microscopy. One or more lasers are sent through a microscope objective at an angle such that they are internally reflected at a glass coverslip. The $\text{W}_{18}\text{O}_{49}$ nanowires catalyze the reactions shown in (b) and (c) to convert non-fluorescent substrate molecules (orange triangles) into fluorescent products (red stars). The fluorescence emission is collected through the same objective and imaged by an electron-multiplying CCD camera. (b) Oxidation of 3'-(p-aminophenyl) fluorescein (APF) by hydroxyl radicals produces fluorescein. (c) Acid-catalyzed condensation of furfuryl alcohol produces fluorescent oligomers.

1
2
3
4
5
6 **Single-molecule super-resolution imaging.** Hydroxyl radicals ($\cdot\text{OH}$) are a key intermediate in
7 several reactions photocatalyzed by metal oxide semiconductors, including water oxidation, the
8 degradation of environmental pollutants, and methane to methanol conversion.^{12-13, 38, 45-47} We
9 hypothesized that differences in the local structure of $\text{W}_{18}\text{O}_{49}$ nanowires would affect their activity
10 for generating $\cdot\text{OH}$ radicals. To image spatial variations in activity along the length of individual
11 $\text{W}_{18}\text{O}_{49}$ nanowires, we first chose a fluorogenic probe that is activated in the presence of $\cdot\text{OH}$
12 radicals (**Figure 2b**). Cleavage of the aminophenyl group of 3'-(p-aminophenyl) fluorescein (APF)
13 by $\cdot\text{OH}$ generates fluorescein.⁴⁸ Control experiments using dispersions of $\text{W}_{18}\text{O}_{49}$ nanowires in
14 solution show that both nanowires containing oxygen vacancies and illumination with photon
15 energies above the band gap of $\text{W}_{18}\text{O}_{49}$ are needed to induce this reaction at the ensemble level
16 (**Figures S13, S14, S15, and S16**). Individual reaction events for single nanowires dispersed on a
17 glass coverslip were then detected using fluorescence microscopy.
18
19
20
21
22
23
24
25
26
27
28
29
30
31
32
33
34
35
36
37
38
39
40
41
42
43
44
45
46
47
48
49
50
51
52
53
54
55
56
57
58
59
60

Single-molecule super-resolution microscopy was conducted using total internal reflection
fluorescence (TIRF) excitation. In this imaging mode, only fluorophores activated near the surface
of the coverslip are detected (**Figure 2a**).^{22-24, 37-38} A 405-nm laser coupled into the objective of
an inverted microscope was used to excite $\text{W}_{18}\text{O}_{49}$ nanowires dispersed on a glass coverslip.
Simultaneous illumination with a 488-nm laser was used to excite the product fluorescein
molecules. After adding a solution of APF (30 nM in a solution of phosphate buffer with pH =
7.4), fluorescence intensity bursts were observed (**Figure 3a**). We attribute these fluorescence
bursts to the generation of fluorescein after reaction with photogenerated $\cdot\text{OH}$ radicals adsorbed
on the surface of the nanowires. We performed the following control experiments to support this
hypothesis. Using APF as a probe, fluorescence signals were not observed on blank coverslips

(i.e., without nanowires, **Figure S25**). Secondly, fluorescence signals were only observed when using both excitation beams (405- and 488-nm). Furthermore, fluorescence signals were not observed when the reaction was carried out in either pure phosphate buffer solution or when dimethyl sulfoxide (DMSO) was added to the solution of APF. DMSO has been previously shown to act as a scavenger for $\cdot\text{OH}$ radicals.^{35, 42} Similar to the ensemble studies, very few fluorescence bursts (a number comparable to a blank sample) were observed for nanowires treated with H_2O_2 to remove oxygen vacancies. Under TIRF excitation, the generation of $\cdot\text{OH}$ radicals in solution using the Fenton reaction (i.e., H_2O_2 and $\text{Fe}(\text{ClO}_4)_2$) did not produce fluorescent bursts, showing that the activation of APF by $\cdot\text{OH}$ radicals occurs on the surface of the nanowires. Finally, simply adding a solution of fluorescein (30 nM in phosphate buffer) to the nanowires did not produce fluorescent bursts, which indicates that fluorescein (which has a higher density of negative charge than APF) does not bind as strongly to the $\text{W}_{18}\text{O}_{49}$ surface as APF. Thus, the turn-off events are attributed to either the desorption of fluorescein from the surface of a $\text{W}_{18}\text{O}_{49}$ nanowire or its decomposition to a non-fluorescent product.

By localizing the positions of individual fluorescence bursts collected over 1500-2500 frames (50 ms exposure), we acquired activity maps for single $\text{W}_{18}\text{O}_{49}$ nanowires with a localization precision of 22 nm (see **Figure S28c** for a histogram of the localization precision). The number of fluorescence bursts localized per nanowire ranged from 130 to 4000 among the 35 nanowires analyzed for this reaction. We did not observe any obvious correlation between morphological irregularities in the nanowires imaged by electron microscopy and the variations in activity imaged by single-molecule fluorescence (**Figure S30**). Furthermore, we kept the imaging short (typically below 5 minutes) to avoid photodegradation of the nanowires. Under the same illumination conditions used for single-molecule fluorescence (405-nm and 488-nm laser, buffer solution

1
2
3 added), thin films of the nanowires showed no obvious structural changes after 5 minutes of
4 irradiation as evidenced by XPS and Raman spectroscopy (see **Figures S11 and S12**). However,
5 we did observe loss of crystallinity in the nanowires after 30 minutes of irradiation. While
6 catalytically active sites, such as oxygen vacancies may diffuse during the time course of these
7 experiments, their diffusion coefficients are too low to observe their mobility over this time
8 period.⁴⁹⁻⁵⁰ **Figure 3c** shows the activity map for photocatalytic •OH radical generation of a
9 representative nanowire, where the color scale indicates the number of fluorescence bursts detected
10 in each accumulation bin ($120 \times 120 \text{ nm}^2$). Significant variations in activity are seen along the
11 W₁₈O₄₉ nanowire, and similar variations were observed for all 35 nanowires imaged (see **Figures**
12 **S26, S31, S32, and S33** in the **Supporting Information** for additional examples).
13
14
15
16
17
18
19
20
21
22
23
24
25
26
27
28
29
30
31
32
33
34
35
36
37
38
39
40
41
42
43
44
45
46
47
48
49
50
51
52
53
54
55
56
57
58
59
60

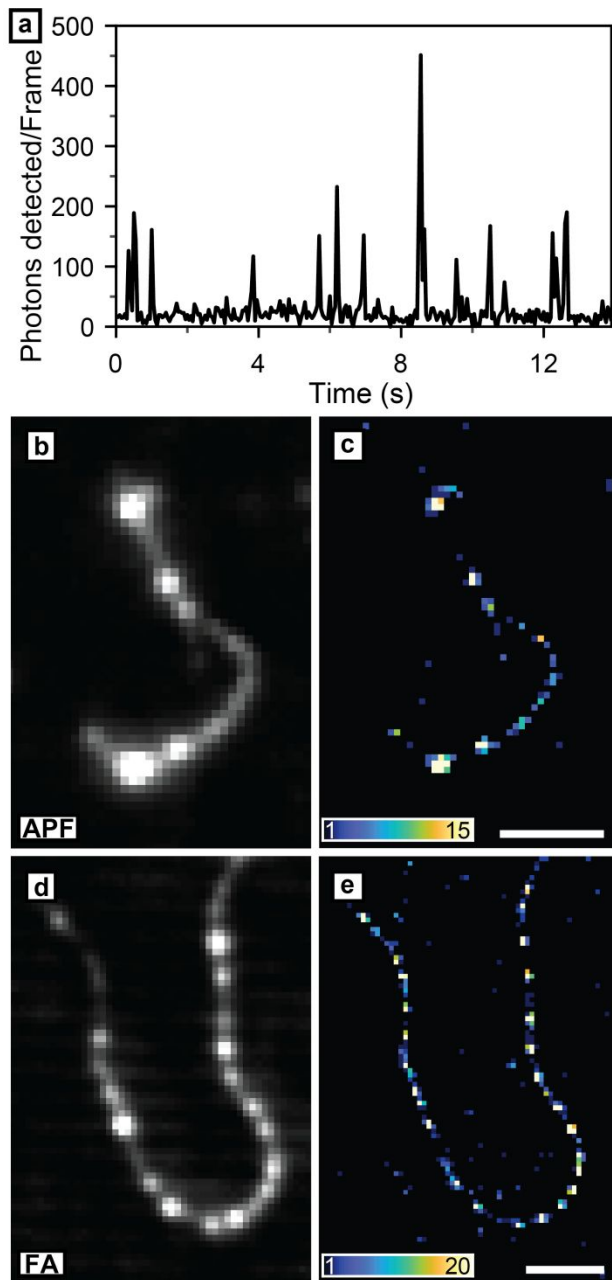


Figure 3. Imaging the catalytic activity of single $\text{W}_{18}\text{O}_{49}$ nanowires. (a) Trajectory of photons detected in a $1 \times 1 \mu\text{m}$ region for a single $\text{W}_{18}\text{O}_{49}$ nanowire using APF as a probe molecule. (b) Diffraction-limited image of a $\text{W}_{18}\text{O}_{49}$ nanowire under the same conditions as in (a). (c) Super-resolution image of the nanowire in (b) containing the positions of all fluorescence bursts. Color scale: number of fluorescence bursts per bin. (d) Diffraction-limited image of a $\text{W}_{18}\text{O}_{49}$ nanowire

1
2
3 using furfuryl alcohol (FA) as a probe molecule. (e) Super-resolution image of the nanowire in
4
5 (d) containing the positions of all fluorescence bursts. Scale bars: 2 μ m.
6
7
8
9
10

11 Tungsten oxide has been used as a solid-acid catalyst, similar to zeolites, due to the presence
12 of both surface oxygen vacancies (**Figure 1c**, top), which act as Lewis acid sites, and surface
13 hydroxyl groups (**Figure 1c**, bottom), which act as Bronsted acid sites.^{11, 51-52} Fourier-transform
14 infrared spectroscopy (FT-IR) of chemically-adsorbed pyridine indicated that dry powders of the
15 W₁₈O₄₉ nanowires possessed both Lewis and Bronsted acid sites (**Figure S10**, and **Table S4**).⁵²
16 Bulk titration of acid sites in the presence or absence of 2,6-dimethylpyridine to selectively poison
17 Bronsted sites gave concentrations of 0.305 mmol of Bronsted sites and 0.110 mmol of Lewis sites
18 per gram of tungsten oxide (see the **Supporting Information** for further experimental details).⁵³⁻
19
20

21 56 However, our single-molecule studies were conducted in an aqueous solution of phosphate
22 buffer with a pH of 7.4. At this pH, hydroxyl groups at the surface of the nanowires are expected
23 to be deprotonated due to the strong acidity of tungsten oxide (pH = 0.34 at the point of zero charge)
24 leading to a negative surface charge on the nanowires.⁵⁷ Consistent with this expectation, zeta
25 potential measurements gave a value of -44.9 ± 0.3 mV (average \pm 1st standard deviation from 3
26 measurements) when the nanowires were dispersed in a buffer solution at a pH of 7.4.
27
28
29
30
31
32
33
34
35
36
37
38
39
40
41
42
43
44
45
46
47
48
49
50
51
52
53
54
55
56
57
58
59
60

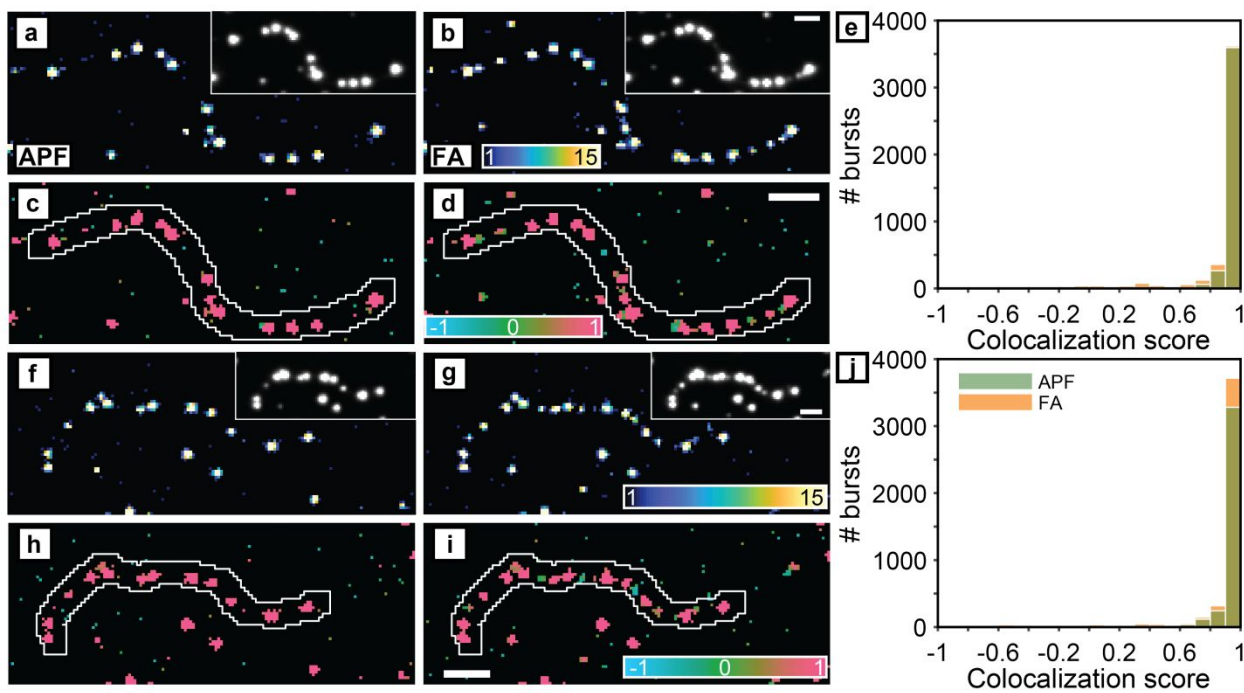


Figure 4. Colocalization of hydroxyl radical generation and Lewis acid sites for two representative $\text{W}_{18}\text{O}_{49}$ nanowires. Super-resolution images of the initial nanowires using (a), (f) APF as a probe to detect hydroxyl radicals and (b), (g) furfuryl alcohol (FA) as a probe to identify Lewis acid sites. Color scale: number of fluorescence bursts per bin. Inset: diffraction-limited images of each imaging condition. Coordinate-based colocalization (CBC) of (c), (h) APF and (d), (i) furfuryl alcohol bursts. Color scale: median colocalization score in each bin ranging from -1 for anti-correlated through 0 for random to +1 for perfectly correlated burst distributions. White lines depict boundaries of the nanowire regions. All scale bars are $2 \mu\text{m}$. The top scale bars apply to the diffraction-limited images in the insets of (a), (b) and (f), (g). The bottom scale bars apply to all super-resolution images in (a)-(d) and (f)-(i). (e), (j) CBC scores for APF (green) and furfuryl alcohol (orange) bursts within the nanowire regions. Segments of other nanowires are seen in each super-resolution image. Only fluorescent bursts detected within the white outlines are included in (e) and (j).

We next selected furfuryl alcohol as a probe molecule that can undergo acid-catalyzed condensation to generate fluorescent oligomers (**Figure 2c**).^{33, 58} The formation mechanism of fluorescent oligomers using both Lewis and Bronsted acids to catalyze this reaction has been previously described,⁵⁹⁻⁶⁰ and tungsten oxide powders have been shown to catalyze the condensation of furfuryl alcohol.⁵⁸ Similar to the conditions used for APF, only Lewis acid sites are expected to be active in the as-synthesized $W_{18}O_{49}$ nanowires as surface hydroxyl groups will be deprotonated at a pH of 7.4. As this reaction does not require photoexcitation of the nanowires, TIRF excitation with a 561-nm laser (*i.e.*, below the bandgap energy of $W_{18}O_{49}$) was used to detect the oligomeric products. After addition of furfuryl alcohol, video recordings showed fluorescence intensity bursts similar to the case of APF (**Figure S29a**). These intensity bursts were not observed on blank coverslips in the same solution (**Figure S25**). **Figure 3e** shows a representative activity map, revealing that the $W_{18}O_{49}$ nanowires also displayed variations in activity along their length for this acid-catalyzed reaction. Similar variations in activity were observed for all 35 nanowires imaged using furfuryl alcohol as a probe molecule (see **Figures S26, S31, S32, and S33** for additional examples).

Coordinate-based colocalization. To directly correlate the active regions for photocatalytic $\cdot OH$ radical generation with the distribution of Lewis acid sites, we sequentially performed single-molecule imaging with both APF and furfuryl alcohol as probe molecules on the same $W_{18}O_{49}$ nanowires (**Figure 4a** and **f** for APF and **Figure 4b** and **g** for furfuryl alcohol). Control experiments showed that APF used in the first round of imaging did not lead to fluorescent contamination during sequential imaging with the furfuryl alcohol probe (see the **Supporting**

1
2
3 **Information and Figure S34** for further discussion). We used a coordinate-based colocalization
4 (CBC) algorithm⁶¹ to quantify the spatial correlation of each fluorescent burst from the two probes,
5 yielding a value ranging from -1 for anti-correlated, through zero for random, to +1 for perfectly-
6 correlated distributions. The colocalization maps (**Figure 4c, d, h and i**) and the distribution of
7 the CBC score across the entire nanowires (**Figure 4e and j**) show that the regions of each
8 nanowire that are more active for generating •OH radicals are also more active for the condensation
9 of furfuryl alcohol. **Figures S31, S32, and S33** provide additional examples of this colocalization
10 analysis performed on the initial W₁₈O₄₉ nanowires. CBC analysis of 33 nanowires shows a high
11 degree of colocalization between the two fluorogenic probes. Thus, not only is the catalytic
12 activity heterogeneous along the lengths of individual nanowires, but to a large extent the same
13 segments within each nanowire are active for both reactions. The number of active regions along
14 each nanowire is much lower than the bulk concentration of oxygen vacancies determined by acid
15 titration, suggesting that clusters of vacancies rather than isolated defects are responsible for higher
16 activity. Evidence that the crystallinity of the nanowires varies along their length comes from
17 HRTEM images of different segments of the same nanowire (**Figure S2**).
18
19

20 As regions containing surface-oxygen vacancies (*i.e.*, Lewis acid sites) are active for both
21 hydroxyl-radical generation and furfuryl-alcohol condensation, changing the availability of these
22 sites should alter the catalytic activity of the nanowires. On the other hand, the availability of
23 Bronsted acid sites should affect only the condensation reaction. To test this hypothesis, we
24 applied different chemical modifications to the W₁₈O₄₉ nanowires and measured their resulting
25 photocatalytic activity at both the ensemble and single-particle level. We first oxidized the W₁₈O₄₉
26 nanowires using H₂O₂ to remove oxygen vacancies, similar to previous reports.⁷ The x-ray
27 diffraction pattern of the oxidized W₁₈O₄₉ nanowires was indistinguishable from the original
28
29
30
31
32
33
34
35
36
37
38
39
40
41
42
43
44
45
46
47
48
49
50
51
52
53
54
55
56
57
58
59
60

1
2
3 pattern (**Figure S5**). However, the diffuse reflectance spectrum (**Figure S4**) of the oxidized
4 nanowires showed significantly reduced absorption at long wavelengths (600 to 2000 nm). XPS
5 showed both a decrease in the intensity of peaks corresponding to W^{4+} and W^{5+} as well as a
6 decrease in surface-adsorbed oxygen species (**Figures S8, S9** and **Table S3**). Hydrogen peroxide
7 adsorbed on the surface of the nanowires was not detected by FT-IR spectroscopy (**Figure S7**).
8 FT-IR spectra measured for dry powders of the nanowires after pyridine adsorption showed a
9 decrease in the intensity of the peaks corresponding to Lewis acid sites, while the peaks
10 corresponding to Bronsted acid sites did not change significantly (**Figure S10**). The zeta potential
11 after oxidation (-42.1 ± 7.32 mV) was similar to the nanowires before oxidation (-44.9 ± 0.3 mV),
12 indicating that the density of deprotonated surface hydroxyl groups did not change significantly.
13 Similarly, acid titration of the oxidized nanowires gave a slightly reduced concentration of
14 Bronsted acid sites (0.229 mmol per gram of tungsten oxide) compared to the initial nanowires
15 (0.305 mmol/g), but a significantly decreased concentration of Lewis acid sites (0.003 vs. 0.110
16 mmol/g). Together, these results demonstrate that the oxidation of the $W_{18}O_{49}$ nanowires using
17 H_2O_2 decreases both the concentration of oxygen vacancies and the availability of Lewis acid sites
18 but does not significantly change the availability of Bronsted acid sites.
19
20

21 We next treated both the initial and oxidized $W_{18}O_{49}$ nanowires with polyvinylpyrrolidone
22 (PVP), a polymeric surfactant frequently used in the synthesis and assembly of metal and metal
23 oxide nanoparticles.⁶²⁻⁶⁴ PVP aids in the colloidal stability and dispersibility of metal oxide
24 particles. Tungsten oxide nanowires with PVP on their surface have been used as photocatalysts
25 and electrocatalysts,⁶⁵⁻⁶⁶ but the effect of the PVP coating on their activity has not been studied.
26 After functionalization, XPS of the nanowires showed an increase in the signal from surface-
27 adsorbed oxygen species without significant changes in the distribution of oxidation states for
28
29
30
31
32
33
34
35
36
37
38
39
40
41
42
43
44
45
46
47
48
49
50
51
52
53
54
55
56
57
58
59
60

tungsten (**Figures S8, S9** and **Table S3**). FT-IR spectra of the PVP-functionalized nanowires after pyridine adsorption displayed weaker and broader peaks for both Bronsted acid and Lewis acid sites (**Figure S10** and **Table S4**), indicating that PVP was bound to both sites. In aqueous solution, the binding of PVP to surface-hydroxyl groups can suppress deprotonation of the Bronsted acid sites. Evidence for this suppression is provided by differences in the zeta potential of the two samples. While the zeta potential was between -42 and -45 mV for the initial and oxidized nanowires before PVP treatment, it dropped to -8.4 ± 0.7 mV (average \pm 1st standard deviation from 3 measurements) for the initial nanowires and to -5.6 ± 5.6 mV for the oxidized nanowires after functionalization with PVP.

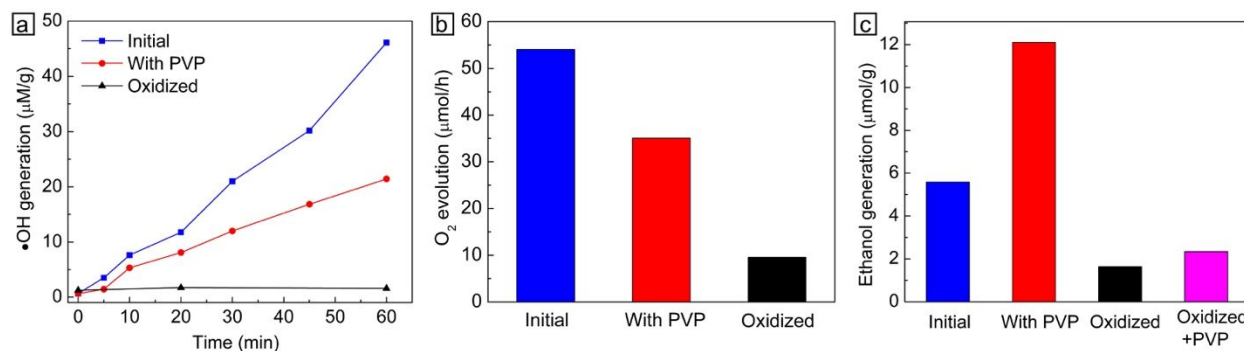


Figure 5. Ensemble catalytic activity of $\text{W}_{18}\text{O}_{49}$ nanowires. (a) The rate of photocatalytic $\bullet\text{OH}$ generation for the initial $\text{W}_{18}\text{O}_{49}$ nanowires (blue squares), oxidized nanowires (black triangles), and PVP-functionalized nanowires (red circles) as measured by the reaction between $\bullet\text{OH}$ and coumarin to produce fluorescent umbelliferone. (b) Rate of O_2 evolution for different nanowire samples during photocatalytic H_2O oxidation. (c) Amount of ethanol produced by different nanowire samples after the acid-catalyzed condensation of ethyl acetate for 24 hours.

1
2
3 Both APF and coumarin were used as fluorogenic probes to measure the rates of photocatalytic
4 hydroxyl radical generation (see **Supporting Information** for further details) using dispersions of
5 W₁₈O₄₉ nanowires in solution. Coumarin reacts with •OH radicals to generate the highly
6 fluorescent umbelliferone (**Figure S17**).⁴⁵⁻⁴⁶ As shown in **Figure 5a**, the initial W₁₈O₄₉ nanowires
7 produced •OH radicals at a greater rate compared to the ones functionalized with PVP. Nanowires
8 oxidized with H₂O₂ produced a negligible amount of •OH radicals (see also **Figures S16** and **S19**).
9 Removing oxygen vacancies via thermal annealing of the nanowires in air also gave negligible
10 activity for •OH generation. We next tested the activity of the different nanowire samples for both
11 photocatalytic water oxidation and the degradation of Rhodamine B as these reactions rely on the
12 generation of •OH radicals.^{38, 45-47} As shown in **Figure 5b**, the initial nanowires showed the
13 highest rate of oxygen evolution. PVP treatment led to a moderate reduction in activity, and
14 oxidizing the nanowires led to a significant reduction in their activity for water oxidation. Similar
15 activity trends were observed for the photocatalytic degradation of Rhodamine B (**Figures S20**
16 and **S21**). These ensemble measurements show that oxygen vacancies are necessary for
17 photocatalytic activity in agreement with previous studies.^{3-11, 17-19}

18
19
20
21
22
23
24
25
26
27
28
29
30
31
32
33
34
35
36
37
38 Different mechanisms have been proposed to explain the increased photocatalytic activity for
39 metal oxide nanocrystals containing oxygen vacancies. These mechanisms include changes in the
40 electronic structure induced by oxygen vacancies that lead to a narrowing of the band gap,^{4, 10}
41 absorption enhancement through the sub-band gap, free carrier absorption,^{5, 16} and the activation
42 of molecules adsorbed onto metal ions exposed by oxygen vacancies.^{7, 10-11} The high degree of
43 colocalization between •OH radical generation and the presence of oxygen vacancies imaged by
44 single-molecule fluorescence reveals that regions containing oxygen vacancies are active sites for
45 water oxidation. Previous DFT calculations show that an H₂O molecule will preferentially bind
46
47
48
49
50
51
52
53
54
55
56
57
58
59
60

1
2
3 to a tungsten ion exposed by an oxygen vacancy at the (001) surface of WO_3 , which activates the
4 H_2O molecule towards dissociation to H^+ and OH^- .⁶⁷⁻⁷⁰ An adsorbed OH^- ion can then be oxidized
5 to an $\cdot\text{OH}$ radical using photoexcited holes in the metal oxide.⁷¹ These previous computational
6 studies examined activation of water at isolated oxygen vacancies. Our results indicate that
7 clusters of oxygen vacancies form the catalytically active regions along $\text{W}_{18}\text{O}_{49}$ nanowires.
8
9
10
11
12
13

14
15 While PVP lowered the activity of the nanowires for the photocatalytic reactions described
16 above, it increased their activity for acid-catalyzed reactions not requiring photoexcitation. As the
17 condensation of furfuryl alcohol produces a complex distribution of products,⁵⁹⁻⁶⁰ we used the
18 acid-catalyzed hydrolysis of ethyl acetate in aqueous solution to compare the activity of different
19 nanowires.⁷²⁻⁷³ Oxidized nanowires, in which Lewis acid sites had been removed, produced a
20 lower amount of ethanol than the initial nanowires (**Figure 5c**). However, PVP functionalization
21 increased the relative activity of both the initial and oxidized nanowires. To further examine the
22 role of PVP in modifying the surface of the nanowires, we used DFT to calculate the binding
23 energy of a PVP monomer to different surface sites of tungsten oxide (see the **Supporting**
24 **Information** for details of the calculations). For ease of calculation, we used a slab of WO_3
25 exposing the (001) surface, similar to previous studies.^{67-70, 74} While the $\text{W}_{18}\text{O}_{49}$ structure is more
26 complex, the (001) facets of both $\text{W}_{18}\text{O}_{49}$ and WO_3 contain W–O bonds normal to the surface
27 allowing us to look at the interaction of a PVP monomer unit to either a single oxygen vacancy
28 (*i.e.*, Lewis acid site) or hydroxyl group (*i.e.*, Bronsted acid site). The strongest binding
29 interactions were found between the electron-donating atoms of the PVP monomer and Lewis acid
30 sites (*i.e.*, -2.1 eV for binding via the O atom of PVP and -1.9 eV for binding via the N atom, see
31 **Figure S23** and **Table S2**). The lower activity observed for PVP-treated nanowires in reactions
32 requiring photocatalytic $\cdot\text{OH}$ generation arises from competitive binding of the polymer to these
33
34
35
36
37
38
39
40
41
42
43
44
45
46
47
48
49
50
51
52
53
54
55
56
57
58
59
60

1
2
3 surface sites. Hydrogen bonding of the PVP monomer to a surface hydroxyl group was also
4 favorable (*i.e.*, -0.9 eV for binding via the O atom of PVP and -0.8 eV for binding via the N atom).
5
6 While the hydrogen bonding interaction was weaker than binding to an oxygen vacancy, it was
7 stronger than the PVP monomer binding to a deprotonated hydroxyl group (*i.e.*, -0.6 eV between
8 the deprotonated surface O atom and the carbonyl C atom of PVP). Thus, hydrogen bonding of
9 PVP to surface hydroxyl groups appears to suppress their deprotonation at neutral pH, which is
10 supported by the lower surface charge observed for PVP-treated nanowires. Dynamic hydrogen
11 bonding of monomer units along the PVP polymer would allow Bronsted acid sites to still be
12 available for the acid-catalyzed condensation of ethyl acetate consistent with the higher activity
13 seen for PVP-treated nanowires. In the future, incorporating the effects of different configurations
14 of PVP oligomers could provide more accurate estimates of PVP binding to different surface sites
15 of tungsten oxide.⁷⁵⁻⁷⁶

16
17
18
19
20
21
22
23
24
25
26
27
28
29

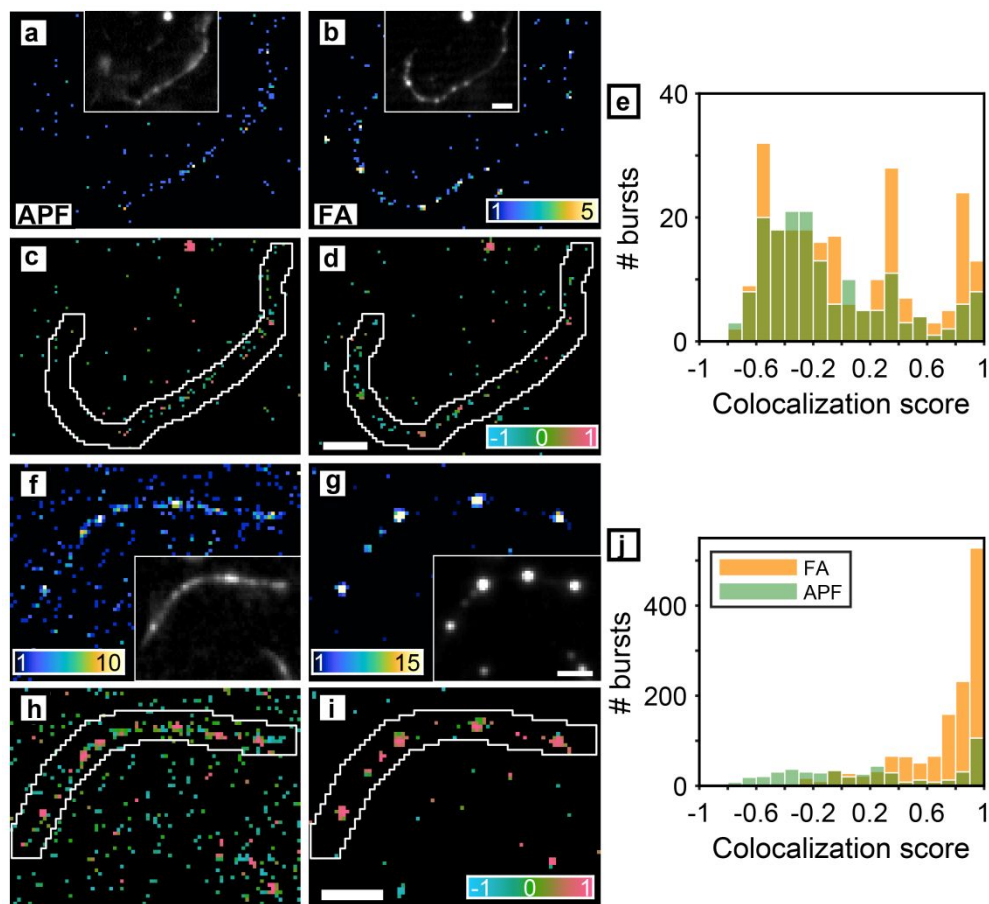


Figure 6. Colocalization of hydroxyl radical generation and Lewis acid sites for PVP-functionalized $\text{W}_{18}\text{O}_{49}$ nanowires. Super-resolution images of the nanowires using (a), (f) APF as a probe to detect hydroxyl radicals and (b), (g) furfuryl alcohol (FA) as a probe to identify Lewis and Bronsted acid sites. Color scale: number of fluorescence bursts per bin. Inset: diffraction-limited images of each imaging condition. Coordinate-based colocalization (CBC) of (c), (h) APF and (d), (i) furfuryl alcohol bursts. Color scale: median of the colocalization score in each bin, ranging from -1 for anti-correlated through 0 for random to +1 for perfectly-correlated burst distributions. White lines depict boundaries of the nanowire regions. All scale bars are 3 μm . The top scale bars apply to the diffraction-limited images in the insets of (a), (b) and (f), (g). The bottom scale bars apply to all super-resolution images in (a)-(d) and (f)-(i). (e), (j) CBC scores for

1
2
3 APF (green) and furfuryl alcohol (orange) bursts within the nanowire regions. Segments of other
4 nanowires are seen in each super-resolution image. Only fluorescent bursts detected within the
5 white outlines are included in (e) and (j).
6
7
8
9
10
11
12
13

14 The ensemble changes in photocatalytic activity described above arise from the activation or
15 deactivation of different sites on the nanowires. We next conducted the same correlative, single-
16 molecule imaging on PVP-functionalized $W_{18}O_{49}$ nanowires using both APF and furfuryl alcohol
17 as probes. **Figure 6a, b, f and g** show the activity maps for both $\cdot OH$ radical generation and
18 furfuryl alcohol condensation obtained by localizing all fluorescence bursts. While they are
19 strongly correlated in the initial nanowires (**Figure 4e and j**), PVP treatment consistently reduced
20 the correlations between APF and FA localizations (**Figure 6c-e and h-j**), as reflected by a broader
21 range of CBC scores (see **Figures S36 and S37** for additional examples). Accumulating the CBC
22 scores across all 33 initial nanowires (**Figure 7a and b**) versus all 40 PVP-functionalized
23 nanowires (**Figure 7c and d**) shows that PVP treatment simultaneously reduces the CBC scores
24 for both species within each nanowire and increases the heterogeneity of CBC scores across
25 nanowires (**Figure 7e**). Specifically, the per-nanowire CBC scores of APF (0.92 ± 0.08 , average
26 $\pm 1^{\text{st}}$ standard deviation of median CBC score) and FA (0.89 ± 0.13) for the initial nanowires
27 dramatically reduce to 0.19 ± 0.33 for APF and 0.54 ± 0.37 for FA for the PVP-functionalized
28 ones (**Figure 7e**). Moreover, the heterogeneous effects of PVP functionalization are evidenced by
29 the increased variation in CBC scores across nanowires after the treatment. We also attempted
30 colocalization analysis for the oxidized nanowires. Similar to the low ensemble activity shown in
31 **Figure 5**, the number of fluorescent bursts generated by the oxidized nanowires was reduced for
32 both probe reactions to a level comparable to the background. Interestingly, after functionalizing
33
34
35
36
37
38
39
40
41
42
43
44
45
46
47
48
49
50
51
52
53
54
55
56
57
58
59
60

1
2
3 the oxidized nanowires with PVP, the number of fluorescence bursts for the APF transformation
4 was still low (**Figure S35i**), but the nanowires recovered their activity for FA condensation
5 (**Figure S35ii**).
6
7

8
9 Negative CBC scores seen for localizations in the PVP-functionalized nanowires represent
10 mutually exclusive sites for •OH radical generation and furfuryl-alcohol condensation. The
11 photocatalytic generation of •OH radicals at Lewis acid sites is inhibited after treating the
12 nanowires with PVP. DFT calculations indicate PVP inhibits activity by binding to the tungsten
13 ions exposed by oxygen vacancies, thus blocking these sites for the adsorption of H₂O (**Figure**
14 **S23**). This type of binding is supported by FT-IR spectroscopy (**Figure S10a** and **Table S4**) and
15 the reduced ensemble photocatalytic activity for the PVP-functionalized nanowires seen in **Figure**
16 **5**. On the other hand, the binding of PVP to surface-hydroxyl groups can suppress their
17 deprotonation, such that they become active for the acid-catalyzed condensation of both ethyl
18 acetate and furfuryl alcohol. This mode of binding is also supported by FT-IR spectroscopy and
19 the change in zeta potential after PVP functionalization. The intermediate binding energy
20 calculated for hydrogen bonding between a PVP monomer and a surface hydroxyl group suggests
21 that dynamic PVP binding in solution allows this Bronsted acid site to still protonate FA during
22 the condensation reaction. Thus, we propose that the regions of the nanowire active for FA
23 condensation, but not active for •OH radical generation, expose Bronsted acid sites. Quantitative
24 colocalization analysis of the two fluorogenic probes reveals this nanowire heterogeneity that
25 cannot be observed at the ensemble level.
26
27
28
29
30
31
32
33
34
35
36
37
38
39
40
41
42
43
44
45
46
47
48
49
50
51
52
53
54
55
56
57
58
59
60

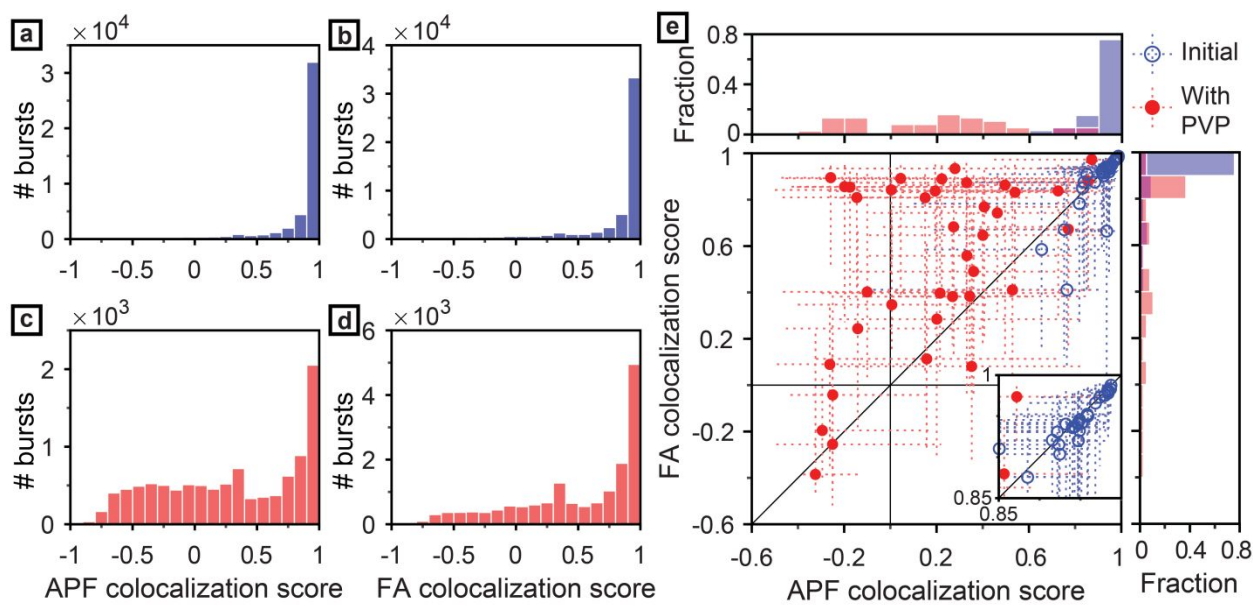


Figure 7. APF and furfuryl alcohol colocalization behavior on initial and PVP-functionalized $\text{W}_{18}\text{O}_{49}$ nanowires. Accumulated (a), (c) APF and (b), (d) furfuryl alcohol (FA) colocalization scores on 33 initial (blue) and 40 PVP-functionalized (red) nanowires. (e) per-wire furfuryl alcohol versus APF colocalization scores for 73 initial and PVP-functionalized nanowires. Open and filled circles are the medians of the CBC scores across each nanowire. Dashed lines show CBC score ranges from 25th to 75th percentile of individual nanowires. Top and right, median APF (top) and furfuryl alcohol (right) CBC scores for each of the initial (blue) and PVP-functionalized (red) nanowires, where counts are given in fractions of the total population.

Conclusions

In summary, tungsten oxide nanowires show significant spatial variations in their catalytic activity. By spatially correlating the nanoscale regions that trigger two fluorogenic probe molecules, we demonstrate that segments containing clusters of oxygen vacancies are more active

1
2
3 for generating hydroxyl radicals. While ensemble measurements can be used to measure average
4 changes in the catalytic activity of a sample after chemical or thermal treatments, through this
5 quantitative colocalization, we demonstrate how new sites become active in a photocatalyst after
6 surface functionalization (*i.e.*, Bronsted acid sites) while others are deactivated (*i.e.*, metal ions
7 bound by PVP) heterogeneously across nanowires. In the future, this method may be used to
8 quantify the spatial correlation for other pairs of reactions, such as the locations of electron and
9 hole extraction in nanostructured photoelectrodes.³⁷
10
11
12
13
14
15
16
17
18
19
20
21
22

23 Experimental Section

24

25
26 **Catalyst preparation.** $\text{W}_{18}\text{O}_{49}$ nanowires were prepared using a hydrothermal method. Tungsten
27 chloride (0.040 g) and 1-butanol (40 mL) were mixed together, transferred to an acid-digestion
28 vessel, and heated at 453 K (180°C) for 24 hours. The product was washed repeatedly with ethanol
29 and dried overnight in a vacuum oven. Oxidation of $\text{W}_{18}\text{O}_{49}$ nanowires was performed by mixing
30 the $\text{W}_{18}\text{O}_{49}$ powder with hydrogen peroxide and 1 M sulfuric acid. The mixture was then washed
31 repeatedly with ethanol and dried overnight. PVP-functionalization of $\text{W}_{18}\text{O}_{49}$ nanowires was
32 carried out by sonicating the $\text{W}_{18}\text{O}_{49}$ powder in an ethanolic solution of PVP. The mixture was
33 then washed repeatedly with ethanol and dried overnight in a vacuum oven at 313 K (40°C).
34
35
36
37
38
39
40
41
42
43
44

45 **Ensemble photocatalytic reactions.** The $\text{W}_{18}\text{O}_{49}$ nanowire powder was dispersed in an aqueous
46 solution of phosphate buffer (pH = 7.4) containing either APF (5 μM) and KIO_3 (10 μM), coumarin
47 (0.1 μM) and KIO_3 (1 μM), or Rhodamine B (5 μM) and KIO_3 (1 μM). The suspension was
48 irradiated with a 405-nm LED while stirring. Aliquots were collected periodically and centrifuged
49
50
51
52
53
54
55
56
57
58
59
60

1
2
3 to remove the nanowires. Fluorescence spectra of the supernatants were then measured in a quartz
4 cuvette using a Cary Eclipse spectrometer.
5
6

7
8 **Photocatalytic water oxidation.** The $W_{18}O_{49}$ nanowire powder (0.02 g) was dispersed in an
9 aqueous solution of 0.1 M KIO_3 . The suspension was then purged with argon for 30 minutes.
10 Photocatalytic water oxidation was performed using a 350 W Xenon lamp under argon flow and
11 stirring of the reaction vessel. For each sample, the amount of O_2 produced was measured every
12 30 minutes using a Shimadzu GC-2014 gas chromatograph.
13
14

15
16 **Acid catalyzed hydrolysis of ethyl acetate.** The $W_{18}O_{49}$ nanowire powder (5 mg) was dispersed
17 in a solution of 1.9 mL of ethyl acetate and 0.1 mL of 0.1 M sodium phosphate buffer (pH = 7).
18 The suspension was sealed and stirred at 60°C for 24 hours. The amount of ethanol generated
19 from each sample was then quantified using a Varian Unity Inova-600 NMR spectrometer.
20
21

22 **Single-molecule fluorescence microscopy with APF and furfuryl alcohol probe molecules.**
23 Glass microscope coverslips were cleaned, rinsed with DI water, and dried under N_2 flow before
24 depositing the $W_{18}O_{49}$ nanowires. A well-dispersed suspension (30 μ L) of the $W_{18}O_{49}$ nanowires
25 in ethanol (10⁻⁴ % w/v) was then spin-coated onto a cleaned coverslip. After drying under N_2 flow,
26 the nanowire-coated coverslip was left in a vacuum oven at 10⁻² atm and room temperature for 30
27 minutes to remove residual solvent.
28
29

30
31 A Nikon N-STORM super-resolution microscopy system with a Nikon CFI-6-APO TIRF 100
32 \times oil-immersion objective lens was used for single-molecule fluorescence imaging. The incident
33 angles of the laser illumination (405 and 488 nm or 561 nm) were adjusted to provide TIRF
34 excitation at the coverslip surface. A quad-band filter set (405/488/561/647, CHROMA,
35 TRF89902-NK) was used to collect emission from the fluorogenic probes, and an Andor iXon 897
36
37
38
39
40
41
42
43
44
45
46
47
48
49
50
51
52
53
54
55
56
57
58
59
60

1
2
3 electron-multiplying CCD with 160 nm effective pixel size was used for imaging. Image stacks
4 of 2500 frames for APF oxidation and 1500 frames for the condensation of furfuryl alcohol were
5 recorded at an exposure time of 50 milliseconds. All measurements were carried out within 15
6 minutes after placing the coverslip on the microscope stage to limit system drift.
7
8

9
10 For imaging the oxidation of APF to produce fluorescein, a solution of 30 nM APF in
11 phosphate buffer (pH = 7.4) with 1 μ M of KIO₃ was dropped onto the coverslip. For this reaction,
12 405-nm and 488-nm lasers were used to photoexcite the W₁₈O₄₉ nanowires and fluorescein,
13 respectively. For imaging the condensation of furfuryl alcohol, 100 μ L of a solution of 10%
14 furfuryl alcohol (v/v) in phosphate buffer was dropped onto the coverslip. A 561-nm laser was
15 used to excite the fluorescent oligomers generated in this reaction. For both reactions, the solutions
16 were purged with argon for 30 minutes before imaging. When imaging both reactions sequentially
17 on the same set of W₁₈O₄₉ nanowires, the oxidation of APF was performed prior to the
18 condensation of furfuryl alcohol to avoid contamination from the deposition of the polymeric
19 product. In between imaging using the two probe molecules, the coverslip was repeatedly washed
20 with phosphate buffer.
21
22

23
24 **Image analysis and colocalization.** All post-processing on the captured images was performed
25 using MATLAB (Mathworks, R2019a) and ImageJ with the ThunderSTORM plugin.⁷⁷ Captured
26 image stacks after offset subtraction using dark images were further background corrected by a
27 temporal quantile filter with 0.4 quantile and 200-frame sliding window (see **Supporting**
28 **Information, Sec. 20 and Figure S24** for further details). Single-molecule bursts in the corrected
29 images were localized by using ThunderSTORM with default settings and custom camera
30 parameters. Only localizations of single molecules with acceptable widths of the fitted point
31 spread function ($80 \text{ nm} < \sigma < 220 \text{ nm}$) were retained for the following process. Detected photons
32
33

1
2
3 per localization were obtained by summing up all photons within a region (5×5 pixels) centered at
4 the localized positions. The estimated localization precision was calculated based on the photons
5 detected and the estimated background as previously described.⁷⁸ Localized single-molecule
6 positions in each frame were grouped across consecutive frames in order to count intensity “bursts”
7 of probe molecules on the nanowires (**Supporting Information, Sec. 21** and **Figures S28 and**
8 **S29**). 2D nanowire activation maps were then visualized by binning all single-molecule bursts
9 within 120×120 nm² bins. Colocalization of APF and furfuryl alcohol super-resolution images
10 was performed using coordinate-based colocalization (CBC) analysis.⁶¹ First, system drift caused
11 by the washing procedure in-between APF and furfuryl alcohol imaging was estimated and
12 removed by measuring shifts in the peaks of the cross-correlation between the diffraction-limited
13 images of the two probes. CBC analysis calculates the colocalization between two super-
14 resolution datasets directly using the localized coordinates of each molecule instead of the
15 pixelized super-resolution reconstructions. Specifically, the spatial density surrounding each burst
16 in the APF dataset was calculated from the neighboring bursts in both the APF and furfuryl alcohol
17 datasets within discs of radius r (from 50 nm to 500 nm in 50 nm steps). The ordered-rank
18 correlation coefficient is calculated using the two sets of the density distributions. Each coefficient
19 was scaled by a weighting factor, depending on the distance to the nearest neighbor, in order to
20 eliminate false positive colocalizations for bursts whose nearest neighbor is far away. The final
21 value was assigned as the colocalization (CBC) score of each burst in the APF dataset, and scores
22 for each burst in the furfuryl alcohol dataset were calculated similarly. Colocalization scores vary
23 from -1, representing perfectly-excluded (anti-correlated) localizations, to +1 for perfectly-
24 colocalized localizations.
25
26
27
28
29
30
31
32
33
34
35
36
37
38
39
40
41
42
43
44
45
46
47
48
49
50
51
52
53
54
55
56
57
58
59
60

1
2
3
4
5
6
7
8
9
10
11
12
13
14
15
16
17
18
19
20
21
22
23
24
25
26
27
28
29
30
31
32
33
34
35
36
37
38
39
40
41
42
43
44
45
46
47
48
49
50
51
52
53
54
55
56
57
58
59
60

Associated Content

Author information.

*email: mdlew@wustl.edu, sadtler@wustl.edu

Notes. The authors declare no competing financial interest.

Supporting Information Available: Additional experimental details on the synthesis of tungsten oxide nanowires, their oxidation, PVP-functionalization, and photoirradiation, additional details on methods used to characterize the structure and morphology of the nanowires, methods used to characterize ensemble catalytic activity, preparation of samples and instrumentation for single-molecule fluorescence microscopy, analysis and processing of super-resolution images and colocalization analysis, and computational methods; Supporting Tables detailing the measurement conditions used for ensemble fluorescence microscopy, the binding energies and bond lengths for a PVP monomer adsorbed onto different sites of tungsten oxide, electron binding energies measured from XPS, peak positions measured from FT-IR, and the burst number, photon count and on-time measured for different nanowires using single-molecule fluorescence microscopy; Supporting Figures providing characterization of different nanowire samples by XRD, XPS, TEM, absorption spectroscopy, FT-IR spectroscopy, and Raman spectroscopy, ensemble fluorescence spectra for different photocatalytic transformations, schemes for different reactions catalyzed by tungsten oxide nanowires, calculated binding configurations of a PVP monomer to tungsten oxide, statistics showing the residual background photons after temporal quantile filtering, additional super-resolution images of tungsten oxide nanowires, region of interest selection for extracting single-molecule bursts, quantitative characterization of APF and furfuryl alcohol blinking events,

1
2
3 colocalization analysis of additional nanowires, and correlation between SEM and fluorescence
4
5 microscopy images. This material is available free of charge via the internet at <http://pubs.acs.org>
6
7
8

9 **Acknowledgements.**

10
11 This material is based upon work supported by the National Science Foundation under grant
12 no. CHE-1753344 to B.S., and under grant no. ECCS-1653777 to M.D.L. Acknowledgment is
13 made to the donors of the American Chemical Society Petroleum Research Fund for partial support
14 of this research (award # PRF58165-DNI10). B.S. and M.D.L acknowledge support from the
15 International Center for Energy, Environment and Sustainability (InCEES) at Washington
16 University. Computational resources were provided by the Extreme Science and Engineering
17 Discovery Environment (XSEDE), which is supported by NSF grants ACI-1053575 and ACI-
18 1548562. STH and RM acknowledge support from NSF DMREF award #1729787. Electron
19 microscopy and x-ray photoelectron spectroscopy were performed at the Institute of Materials
20 Science & Engineering at Washington University. X-ray diffraction was performed in the
21 Department of Earth and Planetary Sciences at Washington University. Zeta potential
22 measurements were performed at the Nano Research Facility at Washington University. The
23 authors thank S. Singamaneni for use of his Raman spectrometer, B. Wieliczka and R. Loomis for
24 use of their absorption spectrometer, J. Lu for helpful discussions, and O. Zhang for technical
25 assistance.
26
27
28
29
30
31
32
33
34
35
36
37
38
39
40
41
42
43
44
45
46
47
48
49
50
51
52
53
54
55
56
57
58
59
60

1
2
3
4
5
References
6
7
8
9
10
11
12
13
14
15
16
17
18
19
20
21
22
23
24
25
26
27
28
29
30
31
32
33
34
35
36
37
38
39
40
41
42
43
44
45
46
47
48
49
50
51
52
53
54
55
56
57
58
59
60

1. Xie, Y. P.; Liu, G.; Yin, L.; Cheng, H.-M., Crystal Facet-Dependent Photocatalytic
2. Oxidation and Reduction Activity of Monoclinic WO_3 for Solar Energy Conversion. *Journal of Materials Chemistry* **2012**, *22*, 6746-6751.
3. Li, R.; Han, H.; Zhang, F.; Wang, D.; Li, C., Highly Efficient Photocatalysts Constructed by Rational Assembly of Dual-Cocatalysts Separately on Different Facets of BiVO_4 . *Energy & Environmental Science* **2014**, *7*, 1369-1376.
4. Chen, X.; Liu, L.; Yu, P. Y.; Mao, S. S., Increasing Solar Absorption for Photocatalysis with Black Hydrogenated Titanium Dioxide Nanocrystals. *Science* **2011**, *331*, 746-750.
5. Lei, F.; Sun, Y.; Liu, K.; Gao, S.; Liang, L.; Pan, B.; Xie, Y., Oxygen Vacancies Confined in Ultrathin Indium Oxide Porous Sheets for Promoted Visible-Light Water Splitting. *Journal of the American Chemical Society* **2014**, *136*, 6826-6829.
6. Yan, J.; Wang, T.; Wu, G.; Dai, W.; Guan, N.; Li, L.; Gong, J., Tungsten Oxide Single Crystal Nanosheets for Enhanced Multichannel Solar Light Harvesting. *Advanced Materials* **2015**, *27*, 1580-1586.
7. Huang, Z.-F.; Song, J.; Pan, L.; Zhang, X.; Wang, L.; Zou, J.-J., Tungsten Oxides for Photocatalysis, Electrochemistry, and Phototherapy. *Advanced Materials* **2015**, *27*, 5309-5327.
8. Xi, G.; Ouyang, S.; Li, P.; Ye, J.; Ma, Q.; Su, N.; Bai, H.; Wang, C., Ultrathin $\text{W}_{18}\text{O}_{49}$ Nanowires with Diameters Below 1 nm: Synthesis, Near-Infrared Absorption, Photoluminescence, and Photochemical Reduction of Carbon Dioxide. *Angewandte Chemie International Edition* **2012**, *51*, 2395-2399.

1
2
3 8. Chen, X.; Zhou, Y.; Liu, Q.; Li, Z.; Liu, J.; Zou, Z., Ultrathin, Single-Crystal WO₃
4 Nanosheets by Two-Dimensional Oriented Attachment toward Enhanced Photocatalytic
5 Reduction of CO₂ into Hydrocarbon Fuels under Visible Light. *ACS Applied Materials &*
6 *Interfaces* **2012**, *4*, 3372-3377.
7
8 9. Liang, L.; Li, X.; Sun, Y.; Tan, Y.; Jiao, X.; Ju, H.; Qi, Z.; Zhu, J.; Xie, Y., Infrared Light-
9 Driven CO₂ Overall Splitting at Room Temperature. *Joule* **2018**, *2*, 1004-1016.
10
11 10. Zhang, N.; Li, X.; Ye, H.; Chen, S.; Ju, H.; Liu, D.; Lin, Y.; Ye, W.; Wang, C.; Xu, Q.; Zhu,
12 J.; Song, L.; Jiang, J.; Xiong, Y., Oxide Defect Engineering Enables to Couple Solar Energy
13 into Oxygen Activation. *Journal of the American Chemical Society* **2016**, *138*, 8928-8935.
14
15 11. Zhang, N.; Li, X.; Liu, Y.; Long, R.; Li, M.; Chen, S.; Qi, Z.; Wang, C.; Song, L.; Jiang, J.;
16 Xiong, Y., Defective Tungsten Oxide Hydrate Nanosheets for Boosting Aerobic Coupling
17 of Amines: Synergistic Catalysis by Oxygen Vacancies and Brønsted Acid Sites. *Small* **2017**,
18 *13*, 1701354-1-10.
19
20 12. Villa, K.; Murcia-López, S.; Andreu, T.; Morante, J. R., Mesoporous WO₃ Photocatalyst for
21 the Partial Oxidation of Methane to Methanol Using Electron Scavengers. *Applied Catalysis*
22 *B: Environmental* **2015**, *163*, 150-155.
23
24 13. Zhu, W.; Shen, M.; Fan, G.; Yang, A.; Meyer, J. R.; Ou, Y.; Yin, B.; Fortner, J.; Foston, M.;
25 Li, Z.; Zou, Z.; Sadtler, B., Facet-Dependent Enhancement in the Activity of Bismuth
26 Vanadate Microcrystals for the Photocatalytic Conversion of Methane to Methanol. *ACS*
27 *Applied Nano Materials* **2018**, *1*, 6683-6691.
28
29 14. Pala, R. A.; Leenheer, A. J.; Licherman, M.; Atwater, H. A.; Lewis, N. S., Measurement of
30 Minority-Carrier Diffusion Lengths Using Wedge-Shaped Semiconductor Photoelectrodes.
31 *Energy & Environmental Science* **2014**, *7*, 3424-3430.
32
33
34
35
36
37
38
39
40
41
42
43
44
45
46
47
48
49
50
51
52
53
54
55
56
57
58
59
60

1
2
3
4
5
6
7
8
9
10
11
12
13
14
15
16
17
18
19
20
21
22
23
24
25
26
27
28
29
30
31
32
33
34
35
36
37
38
39
40
41
42
43
44
45
46
47
48
49
50
51
52
53
54
55
56
57
58
59
60

15. Abdi, F. F.; Savenije, T. J.; May, M. M.; Dam, B.; van de Krol, R., The Origin of Slow
2 Carrier Transport in BiVO₄ Thin Film Photoanodes: A Time-Resolved Microwave
3 Conductivity Study. *The Journal of Physical Chemistry Letters* **2013**, *4*, 2752-2757.
16. Cheng, H.; Kamegawa, T.; Mori, K.; Yamashita, H., Surfactant-Free Nonaqueous Synthesis
2 of Plasmonic Molybdenum Oxide Nanosheets with Enhanced Catalytic Activity for
3 Hydrogen Generation from Ammonia Borane under Visible Light. *Angewandte Chemie
4 International Edition* **2014**, *53*, 2910-2914.
17. Gordon, T. R.; Cagnello, M.; Paik, T.; Mangolini, F.; Weber, R. T.; Fornasiero, P.; Murray,
2 C. B., Nonaqueous Synthesis of TiO₂ Nanocrystals Using TiF₄ to Engineer Morphology,
3 Oxygen Vacancy Concentration, and Photocatalytic Activity. *Journal of the American
4 Chemical Society* **2012**, *134*, 6751-6761.
18. Wang, J.; Wang, Z.; Huang, B.; Ma, Y.; Liu, Y.; Qin, X.; Zhang, X.; Dai, Y., Oxygen
2 Vacancy Induced Band-Gap Narrowing and Enhanced Visible Light Photocatalytic Activity
3 of ZnO. *ACS Applied Materials & Interfaces* **2012**, *4*, 4024-4030.
19. Zhang, N.; Jalil, A.; Wu, D.; Chen, S.; Liu, Y.; Gao, C.; Ye, W.; Qi, Z.; Ju, H.; Wang, C.;
2 Wu, X.; Song, L.; Zhu, J.; Xiong, Y., Refining Defect States in W₁₈O₄₉ by Mo Doping: A
3 Strategy for Tuning N₂ Activation Towards Solar-Driven Nitrogen Fixation. *Journal of the
4 American Chemical Society* **2018**, *140*, 9434-9443.
20. Zhao, Y.; Balasubramanyam, S.; Sinha, R.; Lavrijen, R.; Verheijen, M. A.; Bol, A. A.;
2 Bieberle-Hütter, A., Physical and Chemical Defects in WO₃ Thin Films and Their Impact on
3 Photoelectrochemical Water Splitting. *ACS Applied Energy Materials* **2018**, *1*, 5887-5895.

1
2
3 21. Manthiram, K.; Alivisatos, A. P., Tunable Localized Surface Plasmon Resonances in
4 Tungsten Oxide Nanocrystals. *Journal of the American Chemical Society* **2012**, *134*, 3995-
5 3998.
6
7
8
9
10 22. Xu, W.; Kong, J. S.; Yeh, Y.-T. E.; Chen, P., Single-Molecule Nanocatalysis Reveals
11 Heterogeneous Reaction Pathways and Catalytic Dynamics. *Nature Materials* **2008**, *7*, 992-
12 996.
13
14
15
16 23. Zhou, X.; Andoy, N. M.; Liu, G.; Choudhary, E.; Han, K.-S.; Shen, H.; Chen, P., Quantitative
17 Super-Resolution Imaging Uncovers Reactivity Patterns on Single Nanocatalysts. *Nature
18 Nanotechnology* **2012**, *7*, 237-241.
19
20
21
22
23
24 24. Andoy, N. M.; Zhou, X.; Choudhary, E.; Shen, H.; Liu, G.; Chen, P., Single-Molecule
25 Catalysis Mapping Quantifies Site-Specific Activity and Uncovers Radial Activity Gradient
26 on Single 2D Nanocrystals. *Journal of the American Chemical Society* **2013**, *135*, 1845-1852.
27
28
29
30
31 25. Zhou, X.; Choudhary, E.; Andoy, N. M.; Zou, N.; Chen, P., Scalable Parallel Screening of
32 Catalyst Activity at the Single-Particle Level and Subdiffraction Resolution. *ACS Catalysis*
33
34 2013, *3*, 1448-1453.
35
36
37
38 26. Du, Y.; He, X.; Zhan, Y.; Li, S.; Shen, Y.; Ning, F.; Yan, L.; Zhou, X., Imaging the Site-
39 Specific Activity and Kinetics on a Single Nanomaterial by Microchamber Array. *ACS
40 Catalysis* **2017**, 3607-3614.
41
42
43
44
45 27. Zou, N.; Chen, G.; Mao, X.; Shen, H.; Choudhary, E.; Zhou, X.; Chen, P., Imaging Catalytic
46 Hotspots on Single Plasmonic Nanostructures Via Correlated Super-Resolution and Electron
47 Microscopy. *ACS Nano* **2018**, *12*, 5570-5579.
48
49
50
51
52
53
54
55
56
57
58
59
60

1
2
3 28. Wilson, A. J.; Willets, K. A., Visualizing Site-Specific Redox Potentials on the Surface of
4 Plasmonic Nanoparticle Aggregates with Superlocalization SERS Microscopy. *Nano Letters*
5 2014, 14, 939-945.
6
7 29. Weber, M. L.; Wilson, A. J.; Willets, K. A., Characterizing the Spatial Dependence of Redox
8 Chemistry on Plasmonic Nanoparticle Electrodes Using Correlated Super-Resolution
9 Surface-Enhanced Raman Scattering Imaging and Electron Microscopy. *The Journal of*
10 *Physical Chemistry C* 2015, 119, 18591-18601.
11
12 30. Chen, T.; Chen, S.; Song, P.; Zhang, Y.; Su, H.; Xu, W.; Zeng, J., Single-Molecule
13 Nanocatalysis Reveals Facet-Dependent Catalytic Kinetics and Dynamics of Palladium
14 Nanoparticles. *ACS Catalysis* 2017, 7, 2967-2972.
15
16 31. Chen, T.; Dong, B.; Chen, K.; Zhao, F.; Cheng, X.; Ma, C.; Lee, S.; Zhang, P.; Kang, S. H.;
17 Ha, J. W.; Xu, W.; Fang, N., Optical Super-Resolution Imaging of Surface Reactions.
18 *Chemical Reviews* 2017, 117, 7510-7537.
19
20 32. Roeffaers, M. B. J.; Sels, B. F.; Uji-i, H.; Schryver, F. C. D.; Jacobs, P. A.; De Vos, D. E.;
21 Hofkens, J., Spatially Resolved Observation of Crystal-Face-Dependent Catalysis by Single
22 Turnover Counting. *Nature* 2006, 439, 572-575.
23
24 33. Roeffaers, M. B. J.; De Cremer, G.; Libeert, J.; Ameloot, R.; Dedecker, P.; Bons, A.-J.;
25 Bückins, M.; Martens, J. A.; Sels, B. F.; De Vos, D. E.; Hofkens, J., Super-Resolution
26 Reactivity Mapping of Nanostructured Catalyst Particles. *Angewandte Chemie International*
27 *Edition* 2009, 48, 9285-9289.
28
29 34. Han, R.; Ha, J. W.; Xiao, C.; Pei, Y.; Qi, Z.; Dong, B.; Bormann, N. L.; Huang, W.; Fang,
30 N., Geometry-Assisted Three-Dimensional Superlocalization Imaging of Single-Molecule
31
32
33
34
35
36
37
38
39
40
41
42
43
44
45
46
47
48
49
50
51
52
53
54
55
56
57
58
59
60

1
2
3 Catalysis on Modular Multilayer Nanocatalysts. *Angewandte Chemie International Edition*
4
5 2014, 53, 12865-12869.
6
7

8 35. Xu, W.; Jain, P. K.; Beberwyck, B. J.; Alivisatos, A. P., Probing Redox Photocatalysis of
9 Trapped Electrons and Holes on Single Sb-Doped Titania Nanorod Surfaces. *Journal of the*
10 *American Chemical Society* 2012, 134, 3946-3949.
11
12 36. Tachikawa, T.; Yamashita, S.; Majima, T., Evidence for Crystal-Face-Dependent TiO₂
13 Photocatalysis from Single-Molecule Imaging and Kinetic Analysis. *Journal of the American*
14 *Chemical Society* 2011, 133, 7197-7204.
15
16 37. Sambur, J. B.; Chen, T.-Y.; Choudhary, E.; Chen, G.; Nissen, E. J.; Thomas, E. M.; Zou, N.;
17 Chen, P., Sub-Particle Reaction and Photocurrent Mapping to Optimize Catalyst-Modified
18 Photoanodes. *Nature* 2016, 530, 77-80.
19
20 38. Sambur, J. B.; Chen, P., Distinguishing Direct and Indirect Photoelectrocatalytic Oxidation
21 Mechanisms Using Quantitative Single-Molecule Reaction Imaging and Photocurrent
22 Measurements. *The Journal of Physical Chemistry C* 2016, 120, 20668-20676.
23
24 39. Mao, X.; Liu, C.; Hesari, M.; Zou, N.; Chen, P., Super-Resolution Imaging of Non-
25 Fluorescent Reactions Via Competition. *Nature Chemistry* 2019, 11, 687-694.
26
27 40. Hesari, M.; Mao, X.; Chen, P., Charge Carrier Activity on Single-Particle
28 Photo(Electro)Catalysts: Toward Function in Solar Energy Conversion. *Journal of the*
29 *American Chemical Society* 2018, 140, 6729-6740.
30
31 41. Tachikawa, T.; Yonezawa, T.; Majima, T., Super-Resolution Mapping of Reactive Sites on
32 Titania-Based Nanoparticles with Water-Soluble Fluorogenic Probes. *ACS Nano* 2013, 7,
33 263-275.
34
35
36
37
38
39
40
41
42
43
44
45
46
47
48
49
50
51
52
53
54
55
56
57
58
59
60

1
2
3 42. Ha, J. W.; Ruberu, T. P. A.; Han, R.; Dong, B.; Vela, J.; Fang, N., Super-Resolution Mapping
4 of Photogenerated Electron and Hole Separation in Single Metal–Semiconductor
5 Nanocatalysts. *Journal of the American Chemical Society* **2014**, *136*, 1398-1408.
6
7
8
9
10 43. Li, Y.; Bando, Y.; Golberg, D., Quasi-Aligned Single-Crystalline $W_{18}O_{49}$ Nanotubes and
11 Nanowires. *Advanced Materials* **2003**, *15*, 1294-1296.
12
13
14 44. Guo, C.; Yin, S.; Yan, M.; Kobayashi, M.; Kakihana, M.; Sato, T., Morphology-Controlled
15 Synthesis of $W_{18}O_{49}$ Nanostructures and Their Near-Infrared Absorption Properties.
16
17 *Inorganic Chemistry* **2012**, *51*, 4763-4771.
18
19
20
21 45. Kim, J.; Lee, C. W.; Choi, W., Platinized WO_3 as an Environmental Photocatalyst That
22 Generates OH Radicals under Visible Light. *Environmental Science & Technology* **2010**, *44*,
23
24 6849-6854.
25
26
27
28 46. Zhang, J.; Nosaka, Y., Mechanism of the OH Radical Generation in Photocatalysis with TiO_2
29 of Different Crystalline Types. *The Journal of Physical Chemistry C* **2014**, *118*, 10824-
30
31 10832.
32
33
34
35 47. Lops, C.; Ancona, A.; Di Cesare, K.; Dumontel, B.; Garino, N.; Canavese, G.; Hérnandez,
36 S.; Cauda, V., Sonophotocatalytic Degradation Mechanisms of Rhodamine B Dye Via
37
38 Radicals Generation by Micro- and Nano-Particles of ZnO . *Applied Catalysis B: Environmental* **2019**, *243*, 629-640.
39
40
41
42
43
44 48. Gomes, A.; Fernandes, E.; Lima, J. L. F. C., Fluorescence Probes Used for Detection of
45 Reactive Oxygen Species. *Journal of Biochemical and Biophysical Methods* **2005**, *65*, 45-
46
47 80.
48
49
50
51 49. Sikora, E.; Sikora, J.; Macdonald, D. D., A New Method for Estimating the Diffusivities of
52 Vacancies in Passive Films. *Electrochimica Acta* **1996**, *41*, 783-789.
53
54
55
56
57
58
59
60

1
2
3 50. Vázquez, G.; González, I., Diffusivity of Anion Vacancies in WO_3 Passive Films.
4
5 *Electrochimica Acta* **2007**, *52*, 6771-6777.
6
7 51. Barton, D. G.; Soled, S. L.; Iglesia, E., Solid Acid Catalysts Based on Supported Tungsten
8 Oxides. *Topics in Catalysis* **1998**, *6*, 87-99.
9
10 52. González, J.; Wang, J. A.; Chen, L. F.; Manríquez, M. E.; Dominguez, J. M., Structural
11 Defects, Lewis Acidity, and Catalysis Properties of Mesostructured $\text{WO}_3/\text{SBA-15}$
12 Nanocatalysts. *The Journal of Physical Chemistry C* **2017**, *121*, 23988-23999.
13
14 53. Jacobs, P. A.; Heylen, C. F., Active Sites in Zeolites: III. Selective Poisoning of Bronsted
15 Sites on Synthetic Y Zeolites. *Journal of Catalysis* **1974**, *34*, 267-274.
16
17 54. Oliviero, L.; Vimont, A.; Lavalle, J.-C.; Romero Sarria, F.; Gaillard, M.; Maugé, F., 2,6-
18 Dimethylpyridine as a Probe of the Strength of Brønsted Acid Sites: Study on Zeolites.
19 Application to Alumina. *Physical Chemistry Chemical Physics* **2005**, *7*, 1861-1869.
20
21 55. Hong, J.; Djernes, K. E.; Lee, I.; Hooley, R. J.; Zaera, F., Heterogeneous Catalyst for the
22 Selective Oxidation of Unactivated Hydrocarbons Based on a Tethered Metal-Coordinated
23 Cavitand. *ACS Catalysis* **2013**, *3*, 2154-2157.
24
25 56. Weng, Z.; Yu, T.; Zaera, F., Synthesis of Solid Catalysts with Spatially Resolved Acidic and
26 Basic Molecular Functionalities. *ACS Catalysis* **2018**, *8*, 2870-2879.
27
28 57. Xu, Y.; Schoonan, M. A. A., The Absolute Energy Positions of Conduction and Valence
29 Bands of Selected Semiconducting Minerals. *American Mineralogist* **2000**, *85*, 543-556.
30
31 58. Chan, X.; Nan, W.; Mahajan, D.; Kim, T., Comprehensive Investigation of the Biomass
32 Derived Furfuryl Alcohol Oligomer Formation over Tungsten Oxide Catalysts. *Catalysis
33 Communications* **2015**, *72*, 11-15.
34
35
36
37
38
39
40
41
42
43
44
45
46
47
48
49
50
51
52
53
54
55
56
57
58
59
60

1
2
3 59. Kim, T.; Assary, R. S.; Marshall, C. L.; Gosztola, D. J.; Curtiss, L. A.; Stair, P. C., Acid-
4 Catalyzed Furfuryl Alcohol Polymerization: Characterizations of Molecular Structure and
5 Thermodynamic Properties. *ChemCatChem* **2011**, *3*, 1451-1458.
6
7 60. Choura, M.; Belgacem, N. M.; Gandini, A., Acid-Catalyzed Polycondensation of Furfuryl
8 Alcohol: Mechanisms of Chromophore Formation and Cross-Linking. *Macromolecules*
9 **1996**, *29*, 3839-3850.
10
11 61. Malkusch, S.; Endesfelder, U.; Mondry, J.; Gelléri, M.; Verveer, P. J.; Heilemann, M.,
12 Coordinate-Based Colocalization Analysis of Single-Molecule Localization Microscopy
13 Data. *Histochemistry and Cell Biology* **2012**, *137*, 1-10.
14
15 62. Pattanaik, M.; Bhaumik, S. K., Adsorption Behaviour of Polyvinyl Pyrrolidone on Oxide
16 Surfaces. *Materials Letters* **2000**, *44*, 352-360.
17
18 63. Koczkur, K. M.; Moudrikoudis, S.; Polavarapu, L.; Skrabalak, S. E., Polyvinylpyrrolidone
19 (PVP) in Nanoparticle Synthesis. *Dalton Transactions* **2015**, *44*, 17883-17905.
20
21 64. Wei, J.; Jiao, X.; Wang, T.; Chen, D., Electrospun Photochromic Hybrid Membranes for
22 Flexible Rewritable Media. *ACS Applied Materials & Interfaces* **2016**, *8*, 29713-29720.
23
24 65. Zhou, X.; Qiu, Y.; Yin, J.; Bai, X., High Electrochemical Activity from Hybrid Materials of
25 Electrospun Tungsten Oxide Nanofibers and Carbon Black. *Journal of Materials Science*
26 **2012**, *47*, 6607-6613.
27
28 66. Zhang, H.; Huang, C.; Tao, R.; Zhao, Y.; Chen, S.; Sun, Z.; Liu, Z., One-Pot Solvothermal
29 Method to Synthesize Platinum/W₁₈O₄₉ Ultrafine Nanowires and Their Catalytic
30 Performance. *Journal of Materials Chemistry* **2012**, *22*, 3354-3359.
31
32
33
34
35
36
37
38
39
40
41
42
43
44
45
46
47
48
49
50
51
52
53
54
55
56
57
58
59
60

1
2
3 67. Ping, Y.; Sundararaman, R.; Goddard III, W. A., Solvation Effects on the Band Edge
4 Positions of Photocatalysts from First Principles. *Physical Chemistry Chemical Physics* **2015**,
5 17, 30499-30509.
6
7 68. Liu, L.; Lin, M.; Liu, Z.; Sun, H.; Zhao, X., Density Functional Theory Study of CO₂ and
8 H₂O Adsorption on a Monoclinic WO₃(001) Surface. *Chemical Research in Chinese
9 Universities* **2017**, 33, 255-260.
10
11 69. Zhang, L.; Wen, B.; Zhu, Y.-N.; Chai, Z.; Chen, X.; Chen, M., First-Principles Calculations
12 of Water Adsorption on Perfect and Defect WO₃(0 0 1). *Computational Materials Science*
13 2018, 150, 484-490.
14
15 70. Kishore, R.; Cao, X.; Zhang, X.; Bieberle-Hütter, A., Electrochemical Water Oxidation on
16 WO₃ Surfaces: A Density Functional Theory Study. *Catalysis Today* **2019**, 321-322, 94-99.
17
18 71. Hu, J.; Zhao, X.; Chen, W.; Su, H.; Chen, Z., Theoretical Insight into the Mechanism of
19 Photoelectrochemical Oxygen Evolution Reaction on BiVO₄ Anode with Oxygen Vacancy.
20
21 72. Nakato, T.; Kimura, M.; Nakata, S.-i.; Okuhara, T., Changes of Surface Properties and
22 Water-Tolerant Catalytic Activity of Solid Acid Cs_{2.5}H_{0.5}PW₁₂O₄₀ in Water. *Langmuir* **1998**,
23 14, 319-325.
24
25 73. Koito, Y.; Rees, G. J.; Hanna, J. V.; Li, M. M. J.; Peng, Y.-K.; Puchtler, T.; Taylor, R.; Wang,
26 T.; Kobayashi, H.; Teixeira, I. F.; Khan, M. A.; Kreissl, H. T.; Tsang, S. C. E., Structure–
27 Activity Correlations for Brønsted Acid, Lewis Acid, and Photocatalyzed Reactions of
28 Exfoliated Crystalline Niobium Oxides. *ChemCatChem* **2017**, 9, 144-154.
29
30 74. Albanese, E.; Di Valentin, C.; Pacchioni, G., H₂O Adsorption on WO₃ and WO_{3-x} (001)
31 Surfaces. *ACS Applied Materials & Interfaces* **2017**, 9, 23212-23221.
32
33
34
35
36
37
38
39
40
41
42
43
44
45
46
47
48
49
50
51
52
53
54
55
56
57
58
59
60

1
2
3 75. Zhou, Y.; Saidi, W. A.; Fichthorn, K. A., A Force Field for Describing the
4 Polyvinylpyrrolidone-Mediated Solution-Phase Synthesis of Shape-Selective Ag
5 Nanoparticles. *The Journal of Physical Chemistry C* **2014**, *118*, 3366-3374.
6
7 76. Liu, S.-H.; Saidi, W. A.; Zhou, Y.; Fichthorn, K. A., Synthesis of {111}-Faceted Au
8 Nanocrystals Mediated by Polyvinylpyrrolidone: Insights from Density-Functional Theory
9 and Molecular Dynamics. *The Journal of Physical Chemistry C* **2015**, *119*, 11982-11990.
10
11 77. Ovesný, M.; Křížek, P.; Borkovec, J.; Švindrych, Z.; Hagen, G. M., ThunderSTORM: A
12 Comprehensive ImageJ Plug-in for PALM and STORM Data Analysis and Super-Resolution
13 Imaging. *Bioinformatics* **2014**, *30*, 2389-2390.
14
15 78. Rieger, B.; Stallinga, S., The Lateral and Axial Localization Uncertainty in Super-Resolution
16 Light Microscopy. *ChemPhysChem* **2014**, *15*, 664-670.
17
18
19
20
21
22
23
24
25
26
27
28
29
30
31
32
33
34
35
36
37
38
39
40
41
42
43
44
45
46
47
48
49
50
51
52
53
54
55
56
57
58
59
60

TOC graphic

